

# Surface Accuracy Requirements for Mosaicing at Millimeter Wavelengths

M.A. Holdaway

January 22, 1991

## 1 Introduction

Surface errors on radio dishes cause lower main beam efficiency due to increased sidelobes. The component of the efficiency of an antenna due to surface errors is  $e^{-(4\pi\sigma_{SE}/\lambda)^2}$  (Ruze, 1965), and many antennas are designed with  $\lambda/15$  surfaces or 50% efficiency at the highest frequency of operation. The balance of the power is found in the primary beam (PB) sidelobes. High PB sidelobes are not a problem for most interferometric observations in which the observed object is small compared to the PB and bright sources are not near enough to enter sidelobes. However, any discrepancy between the true antenna PBs and the PB model used in software will lead to errors in a mosaic reconstruction of sources which are large compared to the PB. The required surface accuracy of the antennas is then determined by the required image reconstruction accuracy.

The SNR of a mosaic image subject to pointing errors is expected to be proportional to  $\lambda/D/\sigma_{PE}$ , or the FWHM of the PB over the RMS pointing error. The SNR of a mosaic image subject to primary beam errors will be inversely proportional to the rms PB error. For surface errors which are small compared to the wavelength, the SNR will be proportional to  $(\lambda/\sigma_{SE})^2$ , or the inverse square of the RMS surface error in wavelengths (Cornwell, Holdaway, and Uson, 1992). For very long wavelengths, neither pointing errors nor surface errors are important for mosaicing. While observations of bright sources at short wavelengths will suffer from both surface errors and pointing errors, the effects of surface errors increase more rapidly with decreasing wavelength. A primary goal of this paper is to more accurately determine the interplay between pointing errors and surface errors in mosaic images.

Some relief from pointing errors may be found in pointing selfcalibration for bright sources, or a frequent external pointing calibration. Likewise, the effects of surface errors can be reduced by determining each antenna's voltage pattern holographically or through a primary beam selfcalibration scheme and then reconstructing the image considering each antenna's different voltage pattern. Neither technique has been proven, it is unclear how much will be gained through each technique, and both will require tremendous computer resources if done routinely. We will not consider any improvements

via either of these methods, but we will consider the advantages of using an accurately determined (holographically determined) radially averaged PB which includes the first few sidelobes.

Since both pointing accuracy and surface accuracy will be expensive to achieve and these errors will both be difficult to correct, it is sensible to give pointing and surface accuracy specifications which result in equal levels of error in the mosaic images at some well used frequency such as 230 GHz. It has already been determined that 1''2 pointing permits fairly high quality mosaic images with dynamic range (DR) = 760:1 and fidelity index (FI) = 20 for an array with essentially complete instantaneous Fourier plane coverage (Holdaway, 1990)<sup>1</sup>.

## 2 How to Simulate Surface Errors

In the absence of surface errors, the voltage pattern  $E(\mathbf{x})$  is given by the Fourier transform of the aperture illumination, and the PB is the square modulus of  $E(\mathbf{x})$ . Surface errors introduce phase errors in the incoming wavefront as it reflects from the primary and secondary surfaces and  $E(\mathbf{x})$  is then given by

$$E(\mathbf{x}) = \int f(\mathbf{k}) e^{j4\pi\epsilon(\mathbf{k})/\lambda} e^{j2\pi\mathbf{k}\mathbf{x}} d\mathbf{k} \quad (1)$$

where  $f(\mathbf{k})$  is the aperture illumination,  $\epsilon(\mathbf{k})$  is the surface error distribution,  $\mathbf{k}$  is the antenna plane coordinate, and  $\mathbf{x}$  is the coordinate of the voltage pattern. Given model surface error patterns for each antenna, the voltage pattern and thus the two dimensional primary beam for each antenna may be calculated. The effects of the surface errors on a single visibility point can be simulated by making the Fourier sum of the product of the model brightness distribution and the voltage patterns for the  $i^{th}$  and  $k^{th}$  antennas:

$$V_{i,k}(\mathbf{u}) = \int I(\mathbf{x}) E_i(\mathbf{x}' - \mathbf{x}_i) E_k^*(\mathbf{x}' - \mathbf{x}_k) e^{j2\pi\mathbf{x}\mathbf{u}} d\mathbf{x} \quad (2)$$

where  $\mathbf{x}'$  is related to  $\mathbf{x}$  via a rotation through the parallactic angle of the antenna on the sky and  $\mathbf{x}_i$  is the position on the sky to which the  $i^{th}$  antenna points. Pointing errors are available at no extra computational cost. The cost of performing the surface error simulations is roughly equally divided among the creation of the model voltage patterns (see Section 3), the

---

<sup>1</sup>DR is defined in MMA memo 61 as the peak of the reconstructed image divided by the off-source RMS calculated in two extensive areas close to the image, and FI is calculated by dividing the reconstructed image by the absolute value of the difference between the convolved true brightness distribution and the reconstructed image (Reconstruction/ABS(True\*Beam - Reconstruction)) and taking the median of all pixels greater than 1.5.

rotation of the voltage patterns on the model brightness distribution, and performing the Fourier sum one visibility at a time. In this implementation, the voltage patterns are rotated only to the nearest multiple of  $5^\circ$  to reduce the amount of time spent on the rotation.

### 3 Surface Error Models

The essential step in the surface error simulations is the choice of a realistic surface error model. The form that the surface errors are likely to take will depend on the antenna design and method of construction. We enumerate the following errors:

- **Blockage.** The subreflector will cause central, symmetric blockage, and the feed legs will result in asymmetric blockage. Both sources of blockage will increase the rms sidelobe level, the feed legs leading to asymmetric sidelobes. The effects of the feed legs will be independent of wavelength for wavelengths small compared to the feed legs. The quality of mosaic observations may be limited by the feed legs as  $\lambda/\sigma_{SE}$  becomes large. Calculations indicate that feed legs may increase the rms sidelobe level of the primary beam by only one or two percent of the PB peak, which is small compared to the effects of large, correlated surface errors. The surface error models include one percent central blockage but no feed leg blockage.
- **Panel accuracy.** Each panel will be machined to finite precision. These errors are correlated on very small scales (centimeters or less), and will result in very broad, low level component to the beam. There is a statistically large number of these regions of correlation across the dish, and the resulting affect on the beam will be symmetric. Symmetric distortions of the beam are easily accounted for by holographic measurement of the primary beam. Hence, panel errors have not been considered in these simulations.
- **Panel gaps.** High resolution holographic measurements of antenna surfaces sometimes show gaps between the individual panels (Emerson, 1992, *private communication*). Such errors could be modeled by extending the small scale power law cutoff to smaller scales, but have not been included in our surface error model.
- **Panel setting errors.** The individual panels will imperfectly mimic the ideal paraboloid. These surface errors will be correlated on scales comparable to the panel size (Napier, 1989). Panel setting errors are

a major cause of ill-behaved sidelobes in high frequency observations and are included in the surface error model.

- **Gravitational, thermal, and wind effects** lead to time dependent, large correlation scale surface errors and will be a major contributor to the surface error budget. Surface deviations which change on short scales will tend to average out. Gravitational and thermal effects will vary slowly over the observations. Since observations will be limited to one or two hours from transit due to opacity considerations, time variable surface errors are not considered important in this treatment. Large scale surface errors are included in the model through the power law power spectrum.

The surface errors of existing millimeter interferometer dishes are dominated by panel setting errors and large scale errors, which are addressed in this work by a power law surface error power spectrum. Second order effects have largely been ignored. It may be necessary to perform future surface error simulations with an improved surface error model. Specifically, holographically determined surface error distributions need to be analyzed to determine the surface error power spectrum.

Model A is intended to represent a single piece molded antenna surface and Model B is intended to represent a surface with  $\sim 1$  m panels. As alluded to above, the simulated surface errors are assumed to have a power law power spectrum between an inner and outer cutoff. Model A has surface errors on scales ranging from 4 to 8 meters with a power law of -1.5, and Model B has surface errors on scales ranging from 1 to 8 meters with a somewhat flatter power law of -1.2, or relatively more power on smaller scale surface errors. After random surface errors are generated on a uniformly illuminated circular aperture with 1% central blockage, a plane is fit to and removed from the surface error distribution to eliminate pointing errors, a parabola is fit and removed to eliminate focusing errors, the mean surface error is set to zero, and the rms surface error is scaled to the simulation value. (After massaging the surface in this way, Model A is dominated by astigmatism.) The surface error distribution on the aperture is then converted into a phase error distribution, and the voltage pattern is given by equation 1. Examples of Model A and Model B surface errors are shown in Figures 1 and 2. The corresponding primary beams are shown in Figures 3 and 4, and the primary beam for no surface errors is shown in Figure 5.

Some of the differences between the two surface error models can be quantified in the sky plane. Since Model B has more power on smaller scales than Model A, Model B's PB will have more power in the far out sidelobes. However, Model A will produce a PB with a higher first sidelobe and much higher errors in the main lobe. For rms surface errors of 35 microns



and observing frequency of 230 GHz, Table 1 shows the peak sidelobe level averaged over several different PBs for Model A and Model B. Table 2 shows

Table 1: Average Peak Sidelobe Level PB for Model A and Model B.

Sidelobe	Model A	Model B	Theoretical
1	7.3%	5.0%	2%
2	1.3%	1.5%	—
3	0.7%	1.0%	—

Table 2: Average RMS Error in PB for Model A and Model B.

Surface Error, $\mu\text{m}$	$\lambda/\text{error}$	Model A	Model B
0	$\infty$	0.0004	0.0004
15	87	0.0056	0.0037
25	52	0.0104	0.0066
35	37	0.0166	0.0101
50	26	0.0295	0.0170

the rms difference out to the second null between the PB generated with no surface error and the Model A and Model B PBs averaged over many antennas, as a function of rms surface error. Primary beams with no surface errors were also generated to test the surface error simulation software and these primary beams agree very well with the theoretical primary beam. The rms error between the theoretical PB and the PBs corrupted by the surface errors does not increase with the square of the rms surface error because we are restricting the rms to the region within the second null of the PB and much of the difference beam is far outside of this region.

## 4 Simulations

An optical photograph of an HII region in M31 has been used as the model brightness distribution for these simulations, and a compact array of 39 7.5 meter antennas with high filling factor has been used to determine the Fourier plane sampling (Braun 1989, Holdaway 1990). The observing frequency was set to 230 GHz, the observed declination was 20 degrees to get some parallactic angle change over the observation ( $\sim 20^\circ$ ), and 7 x 7 pointings on the sky separated by  $\lambda/2D$  were each observed for 1 minute

integrations. For both surface error models, data is simulated with rms surface errors of 15, 25, 35, and 50 microns, with identical voltage patterns on all antennas and with different voltage patterns on all antennas, and both without and with 1"2 pointing errors. Identical voltage patterns across the array might result if all antenna surfaces were made from a single mold. (Surface error Model A represents a single piece molded antenna and surface error Model B represents a panelled antenna.) Surface error simulations performed without pointing errors better illuminate the manner in which the surface errors degrade mosaic images, but simulations with both surface errors and pointing errors will be more representative of actual observations.

The simulated data sets have been imaged with the nonlinear mosaic algorithm (Cornwell, 1988). The default choice for the PB used in the mosaic reconstruction is the theoretical PB obtained by squaring the Fourier transform of a uniformly illumination aperture with central blockage. Any instrument which will perform mosaic observations routinely will use an empirical (holographically determined) PB rather than a theoretical PB. Because the PB of AZ-EL mount antennas rotates on the sky, an efficient implementation of the mosaic algorithm requires an azimuthally symmetric beam, so any holographically determined beam must be azimuthally averaged. Hence, the simulated data are imaged with both the theoretical beam and an average of all antennas' PBs:

$$PB_{ave}(r) = \int_0^{2\pi} r d\phi \left( \sum_i^{NPB} E_i(\mathbf{x}) E_i^*(\mathbf{x}) / NPB \right) / 2\pi r. \quad (3)$$

## 5 Simulation Results

The DR and FI for the surface error simulations with no pointing errors are shown in Tables 4 through 7 and the results for simulations with 1"2 pointing errors are shown in Tables 8 through 11. The headings "Same VP" and "Different VP" indicate that a single voltage pattern was used for all antennas and different voltage patterns were used for all antennas, and the reconstruction was performed with the theoretical primary beam. The headings "Same Ave" and "Different Ave" indicate that the data were reconstructed using the average of all antennas' primary beams.

### 5.1 Surface Errors and No Pointing Errors

The MMA proposal specifies that the antenna surface accuracy be  $\lambda/40$  at 1 mm, or 25 microns. Simulations have been performed at 230 GHz with surface errors of 15, 25, 35, and 50 microns. These simulations can be interpreted either as the reconstruction quality at 230 GHz as a function of

antenna surface accuracy, or as reconstruction quality at various frequencies assuming some surface accuracy through  $\lambda/\sigma_{SE}$ . The second interpretation strictly applies only for antennas with dish diameter and surface error correlation lengths scaled by  $\lambda_{obs}/1.3\text{mm}$ , but the 15, 25, 35, and 50 micron simulations will be representative of observations at 2.2 mm, 1.3 mm, 0.93 mm, and 0.65 mm with 25 micron surface errors. Simulations with both surface errors and pointing errors cannot be meaningfully scaled without changing the pointing error.

Recalling the results of the pointing error simulations, the **DR** was  $\sim 40$  times the **FI** indicating that pointing errors caused more problems on source than off source. For surface errors, **DR** is only 5-15 times higher than the **FI**. A linear mosaic error analysis of surface errors (PB errors) indicates that no power should be scattered (high **DR**) and that the **FI** should be limited only by amplitude errors in the source due to the PB errors. What the linear mosaic analysis fails to consider is the different effect the PB errors have on the total power measurements. When the array is pointed towards blank sky but a hefty sidelobe falls on a bright region nearby, the mosaic algorithm is unable to accurately reconstruct a flat base level when the PB model it is using poorly estimates the sidelobe level. As noted above, the antennas' PBs can be averaged to give a better estimate of the sidelobe level, as might be obtained through holography. Imaging the data with the average beam produces greatly improved images in the case of different PBs across the array. In the case where all antennas have the same PB, the averaging scheme reduces to azimuthally averaging a single antenna's PB, resulting in moderate systematic errors as the PB is not rotationally symmetric. Not surprisingly, this technique does not work well when all antennas have the same PB. A logical but costly extension of this line of thought would be to implement a two dimensional array averaged PB which rotates on the sky in the mosaic algorithm. Such a scheme would work very well, and might even be required, if all antennas had the same general surface errors. This all makes comparisons of the different simulations difficult. One must consider the best PB determination, but then we are shortchanging the simulations in which all antennas have the same PB.

When all antennas in the array have different surface error distributions, the **DR** is 2-3 times higher and the **FI** is about 1.5 times higher than the case in which all antennas have the same surface errors, a significantly poorer increase than  $\sqrt{N}$ , or about 6 for 39 antennas. When the average PB is used in the reconstruction, **DR** is 4-6 times higher and **FI** is about 2 times higher for the different antennas case.

The **DR** and **FI** are both 1.5 to 2 times higher for Model B (1 meter surface errors) simulations than for the corresponding Model A simulations. This may be a selection effect of the model brightness distribution we have

chosen: since the model is not very large (5 by 5 pointings not including a guard band), the lower first sidelobe of Model B are an advantage. However, since the far out sidelobes for Model A are lower, this may prove to be an advantage for mosaicing very large sources. Because of the higher level of errors in the main beam and first sidelobe of Model A PB's, it would be necessary to further tighten the surface error specifications if the antenna surfaces were to have very large correlation scales ( $D/2$ ).

Using an average PB in the reconstruction works very well when all antennas are different, increasing the DR by a factor of 2-3. For very low surface errors, this method actually decreases the FI by a modest amount, but the FI is still much higher than 20, the  $1''/2$  pointing error limit. The improvement obtained by using an averaged PB is greater in Model A than Model B because the first sidelobe in Model A is higher. The resulting images using the Model B surface errors is still better than the Model A images. The PB averaging does not work well when all antennas have the same surface errors. A superior reconstruction could be obtained with an implementation of mosaic which manipulated a general 2-D rather than a rotationally symmetric PB.

The linear mosaic error analysis predicts that the SNR of a mosaic image will be proportional to  $(\lambda/\sigma_{SE})^2$ . Figure 6 plots the DR as a function of  $\lambda/\sigma_{SE}$  for MODEL B with no pointing errors both with and without PB averaging. Without PB averaging, DR varies with the 1.85 power of  $\lambda/\sigma_{SE}$ . The dependence of FI on  $\lambda/\sigma_{SE}$  is much flatter, probably because the FI is limited more by deconvolution errors and their interaction with the PB errors. When PB averaging is employed, the power law flattens to a slope of 1.5. The lower slope could be due to deconvolution errors becoming important at higher DR.

## 5.2 Surface Errors with Pointing Errors

When  $1''/2$  pointing errors are added in concert with the range of surface errors presented in the previous simulations, the results are fairly straight forward. Most obvious is the lowering of FI to the 20-30 range. Also the very high DR which were obtained for 15 and 25 micron surface error simulations *without* pointing errors have been clipped at around 1000:1, a bit higher than the DR obtained for  $1''/2$  alone. The surface errors reduce the high PB gradient near the nulls and even eliminate the PB nulls in extreme cases; this could act to alleviate the effects of the pointing errors on the resulting mosaic images. Figure 8 illustrates the behavior of the DR with a range of surface errors and pointing errors. For large surface errors, the results are quite similar to the results without pointing errors in Figure 6. However, as the surface errors decrease the pointing errors limit the DR and force

the curves to flatten out. The slight flattening seen at low surface errors in Figure 6 is probably caused by deconvolution errors beginning to limit the DR.

## 6 Conclusions

Surface errors (or primary beam errors) do not cause particularly bad problems with the on-source image fidelity. However, the dynamic range, determined by measuring off-source errors, is worse than might be expected unless a good primary beam model is determined. Improved beam models lead to substantial increases in the dynamic range but only marginal increases in the on-source fidelity.

If antenna surfaces are made by a molding procedure, the requirements may change: if the correlation scale of the surface errors is on the order of  $D/2$ , then higher surface accuracy is required, around  $\lambda/55$  (assuming the surface errors are not strongly correlated among antennas). On the other hand, if significant power is found in small scale surface errors, less accurate surfaces may be required. If each antenna produced has similar surface error patterns, then it would be necessary to implement 2-D primary beam handling in the mosaic programs or to mount the antennas differently so as to scramble any systematic effects. If molded antenna construction is likely, a new set of simulations should be performed which correctly deals with a general 2-D primary beam.

A main goal for these simulations is to determine if the 25 micron surface accuracy specification is necessary and or sufficient for MMA mosaic observations. As mentioned before, there is not much use in making the surface so good that the effects of the surface errors in the reconstruction are far below the effects of the pointing errors in the reconstruction. We can estimate the DR of observations at different frequencies by interpolating the power laws found in Figures 6 and 7. FI will not be considered because the 1" pointing errors will limit FI up to the highest observable frequency. Consider the best surface error simulation results, obtained from Model B, different surfaces on each antenna, and an improved model PB via PB averaging. Table 11 presents the interpolated DR resulting from 1" pointing errors, 25, 30 and 35 micron surfaces, each at 230 GHz, 350 GHz, and 650 GHz. Any DR less than 505 in the surface error simulations is somewhat suspect as it represents an *extrapolation* rather than an interpolation. Using the "equal error" criteria, the table suggests that 25 micron surfaces are chosen if 650 GHz is the target frequency, 30 micron surfaces are chosen if 350 GHz is the target frequency, and 35 micron surfaces are chosen if 230 GHz is the target frequency. This study depends upon a fairly good PB model being

Table 3: Dynamic Range as a function of frequency and surface error level.

$\nu$ , GHz	1" Pointing	25 $\mu\text{m}$ Surface	30 $\mu\text{m}$ Surface	35 $\mu\text{m}$ Surface
230	800	1400	1090	880
350	570	760	580	450
650	300	290	210	160

easily obtainable. For this reason alone, 25 micron surface accuracy seems to be a good conservative choice. Furthermore, the 25 micron surface accuracy specification was originally made on sensitivity considerations. At this time, mosaicing cannot make a case for more accurate antenna surfaces.

It should be noted that the DR and FI values quoted in this document are somewhat array dependent: arrays with poor  $u, v$  coverage will produce mosaic images in which the errors are dominated by deconvolution errors rather than primary beam errors caused by poor surface accuracy.

MMA Memo 73 (Holdaway, 1992) deals with the very high dynamic range mosaicing of sources dominated by a few bright, compact sources. Primary beam errors and pointing errors cause inconsistencies among the observed fields, which causes FI and DR limitations when the data are deconvolved jointly. Each field may be imaged separately and the brightest features can be removed from the data. Mosaic images constructed from the residual visibilities are still subject to DR and FI limitations, but the brightest features remaining in the image are much weaker, and much higher DR can be achieved by adding the compact features back into the mosaic image. This technique alleviates the imaging limitations imposed by the pointing and surface errors as it can be applied to many of the source morphologies in which the DR is not limited by thermal noise.

## 7 References

- Braun, R. MMA Memo 54, 1989  
 Cornwell, T. J. A. A., 1988.  
 Cornwell, T.J., Holdaway, M.A., and Uson, J.M. *Submitted to A. A.*, 1992.  
 Holdaway, M. A. MMA Memo 61 1990.  
 Holdaway, M. A. MMA Memo 73, 1992.  
 Napier, Peter J., in *Synthesis Imaging in Radio Astronomy*, ed. Perley, Schwab, and Bridle, Astronomical Society of the Pacific, 1989.  
 Ruze, John. *Proc IEEE*, 54, 4, p 633, 1966.

Table 4: Model A, Dynamic Range.

Error, $\mu m$	$\lambda/\sigma_{SE}$	Same VP	Different VP	Same, Ave	Different, Ave
15	87	270	885	430	1675
25	52	135	350	240	900
35	37	85	185	150	580
50	26	50	90	95	335

Table 5: Model B, Dynamic Range.

Error, $\mu m$	$\lambda/\sigma_{SE}$	Same VP	Different VP	Same, Ave	Different, Ave
15	87	540	1635	470	2500
25	52	286	650	240	1400
35	37	181	350	150	885
50	26	106	175	86	505

Table 6: Model A, Fidelity Index.

Error, $\mu m$	$\lambda/\sigma_{SE}$	Same VP	Different VP	Same, Ave	Different, Ave
15	87	50	100	42	72
25	52	28	40	25	53
35	37	18	20	17	41
50	26	12	11	11	28

Table 7: Model B, Fidelity Index.

Error, $\mu m$	$\lambda/\sigma_{SE}$	Same VP	Different VP	Same, Ave	Different, Ave
15	87	71	120	60	86
25	52	47	104	38	71
35	37	35	55	27	61
50	26	23	35	20	47

Table 8: Model A with 1"2 Pointing Errors, Dynamic Range.

Error, $\mu m$	$\lambda/\sigma_{SE}$	Same VP	Different VP	Same, Ave	Different, Ave
15	87	290	850	370	740
25	52	140	385	220	645
35	37	85	185	145	510
50	26	50	90	95	320

Table 9: Model B with 1"2 Pointing Errors, Dynamic Range.

Error, $\mu m$	$\lambda/\sigma_{SE}$	Same VP	Different VP	Same, Ave	Different, Ave
15	87	500	930	420	1050
25	52	275	580	215	950
35	37	170	370	130	760
50	26	110	180	80	500

Table 10: Model A with 1"2 Pointing Errors, Fidelity Index.

Error, $\mu m$	$\lambda/\sigma_{SE}$	Same VP	Different VP	Same, Ave	Different, Ave
15	87	23	21	24	23
25	52	21	25	22	26
35	37	16	20	22	23
50	26	13	13	16	21

Table 11: Model B with 1"2 Pointing Errors, Fidelity Index.

Error, $\mu m$	$\lambda/\sigma_{SE}$	Same VP	Different VP	Same, Ave	Different, Ave
15	87	29	23	37	28
25	52	25	27	29	30
35	37	20	25	24	27
50	26	17	20	20	24



## Figure Captions

Figure 1: An instance of the Model A surface errors.

Figure 2: An instance of the Model B surface errors.

Figure 3: The primary beam obtained from the Model A surface errors scaled to 35 microns ( $\lambda/37$ ).

Figure 4: The primary beam obtained from the Model B surface errors scaled to 35 microns ( $\lambda/37$ ).

Figure 5: The primary beam obtained from a uniformly illuminated blocked aperture with no surface errors. Agreement with the theoretical PB is excellent.

Figure 6: Dynamic Range as a function of  $\lambda/\sigma_{SE}$  for Model B, no pointing errors, with and without PB averaging.

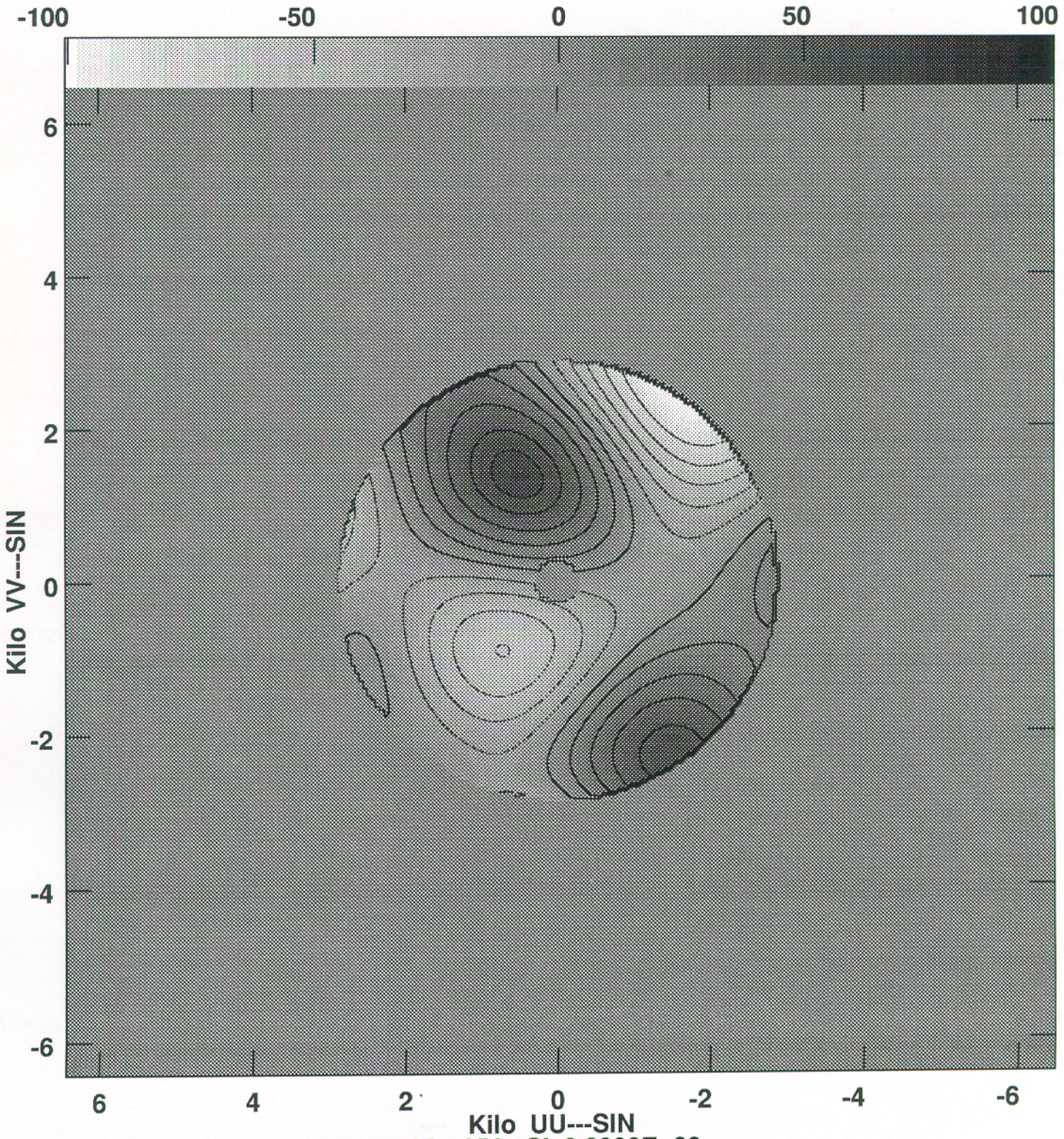
Figure 7: Dynamic Range as a function of  $\theta_{FWHM}/\sigma_{PE}$ .

Figure 8: Dynamic Range as a function of  $\lambda/\sigma_{SE}$  for Model B, 1''2 pointing errors, with and without PB averaging.



Figure 1

Plot file version 1 created 13-DEC-1991 14:36:50  
NONE RA 00 02 45.213 DEC 34 25 48.92 SURF.A.1



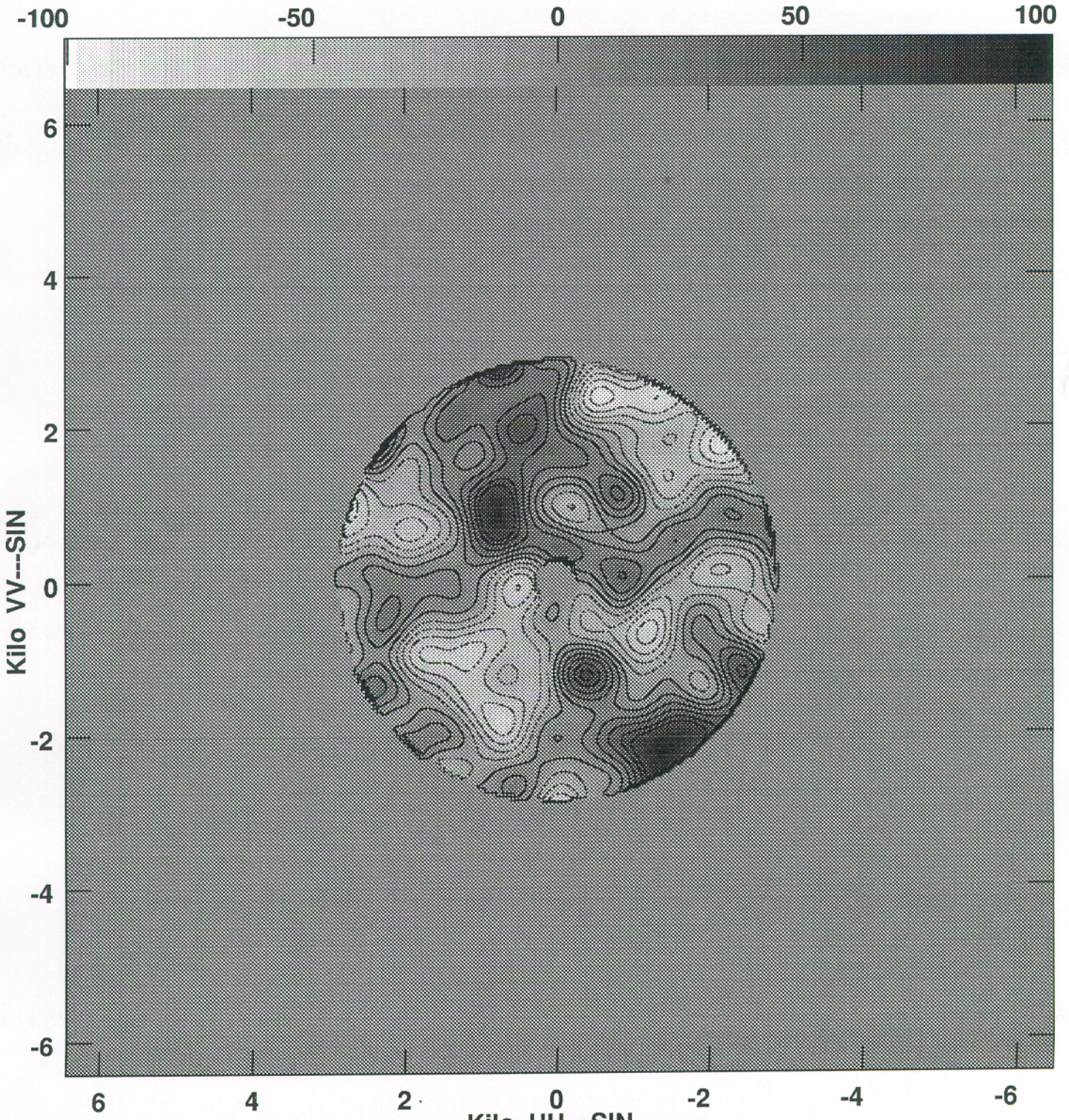
Center at UU---SI 0.0000E+00 VV---SI 0.0000E+00  
Grey scale flux range= -100.0 100.0 MicromETERS  
Peak contour flux = -9.8726E-05 METERS  
Levs = 1.0000E-06 \* ( -75.0, -60.0, -45.0,  
-30.0, -15.0, 1.000, 15.00, 30.00, 45.00,  
60.00, 70.00)



Figure 2

Plot file version 1 created 13-DEC-1991 14:36:34

NONE RA 00 02 45.213 DEC 34 25 48.92 SURF.B.1



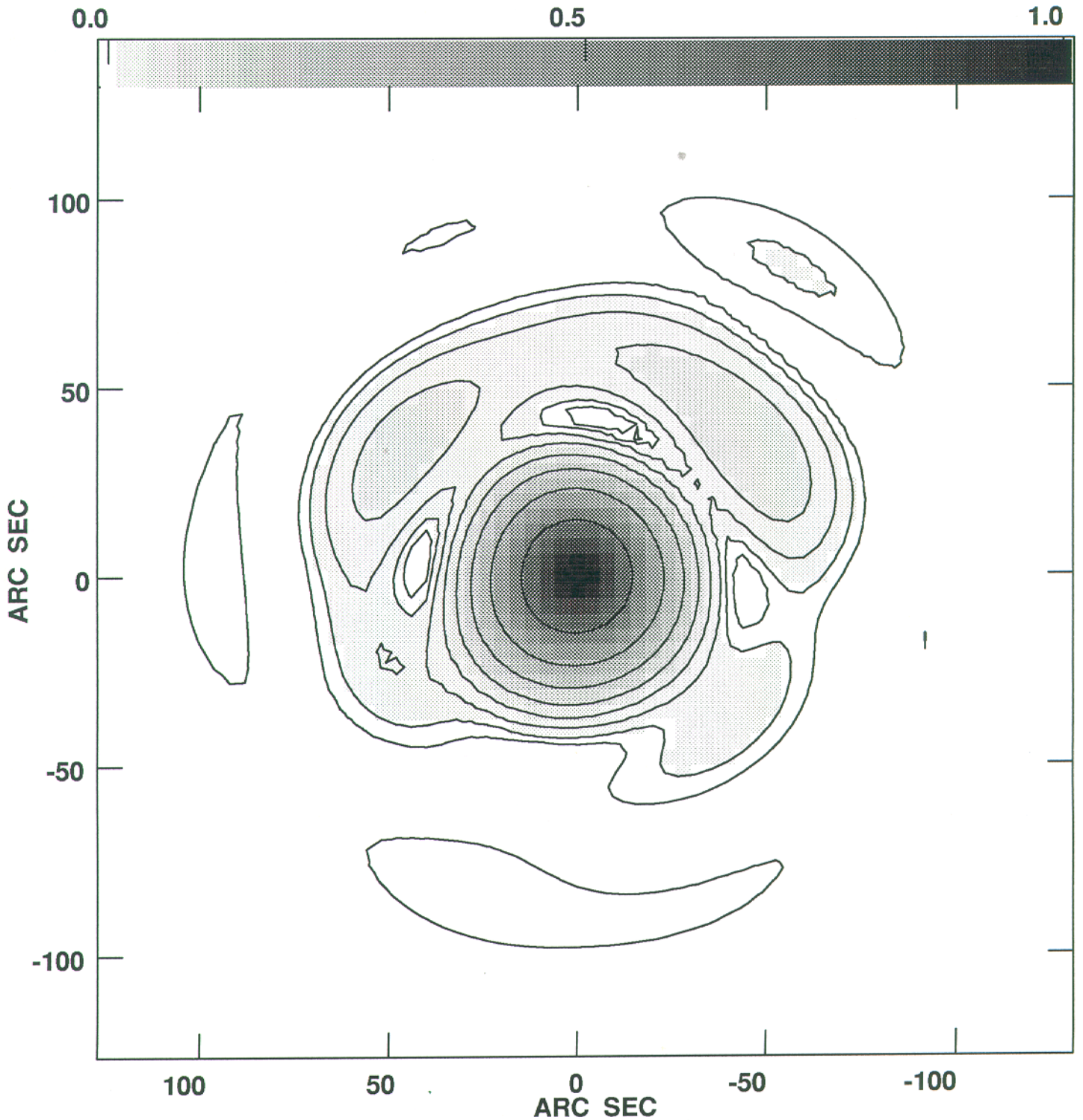
Center at UU---SI 0.0000E+00 VV---SI 0.0000E+00  
Grey scale flux range= -100.0 100.0 MicromETERS  
Peak contour flux = 9.5786E-05 METERS  
Levs = 1.0000E-06 \* ( -75.0, -60.0, -45.0,  
-30.0, -15.0, 1.000, 15.00, 30.00, 45.00,  
60.00, 70.00)



Figure 3

Plot file version 1 created 13-DEC-1991 14:37:07

NONE 2.3000E+11 HZ S35A.PB.1

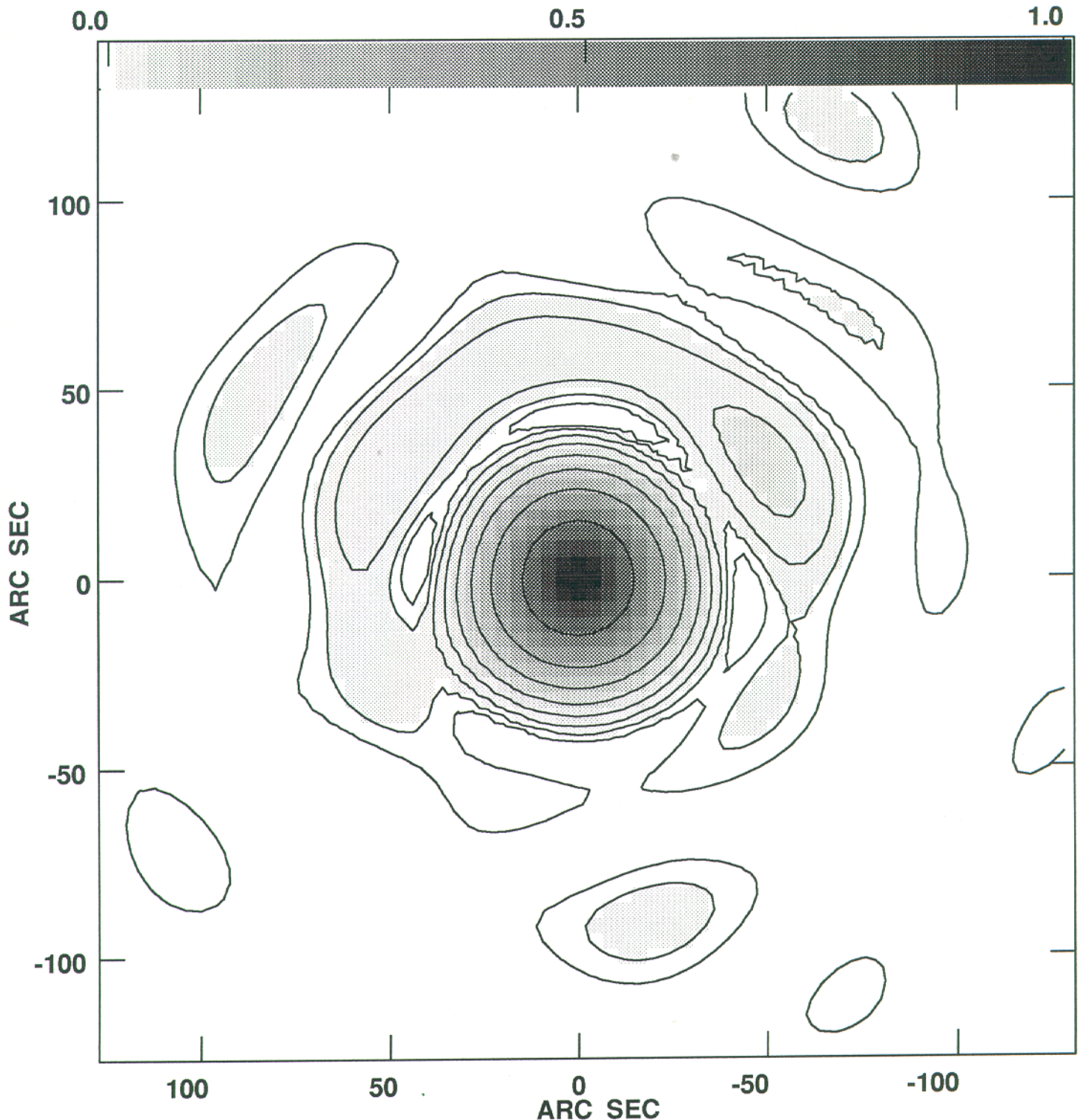


Center at RA 00 00 0.00 DEC 35 00 0.00  
Grey scale flux range= 0.000 1.000  
Peak contour flux = 1.0000E+00  
Levs = 1.0000E-03 \* ( 5.000, 10.00, 20.00,  
40.00, 80.00, 160.0, 320.0, 640.0)

Figure 4

Plot file version 1 created 13-DEC-1991 14:37:24

NONE 2.3000E+11 HZ S35B.PB.1



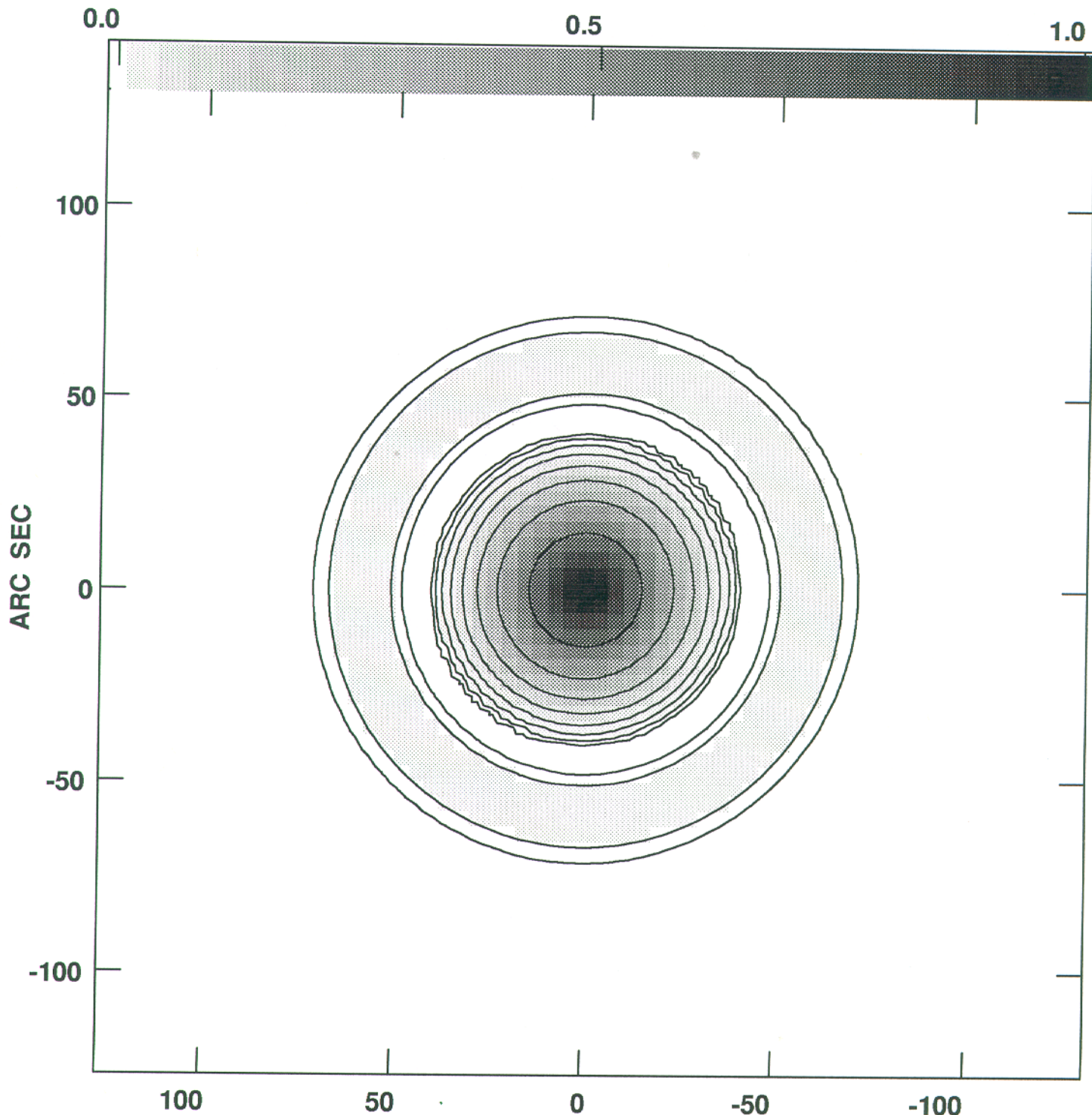
Center at RA 00 00 0.00 DEC 35 00 0.00  
Grey scale flux range= 0.000 1.000  
Peak contour flux = 1.0000E+00  
Levs = 1.0000E-03 \* ( 5.000, 10.00, 20.00,  
40.00, 80.00, 160.0, 320.0, 640.0)



Figure 5

Plot file version 1 created 13-DEC-1991 14:37:41

NONE 2.3000E+11 HZ AIRY.PB.1



Center at RA 00 00 0.000 DEC 35 00 0.00  
Grey scale flux range= 0.000 1.000  
Peak contour flux = 1.0000E+00  
Levs = 1.0000E-03 \* ( 5.000, 10.00, 20.00,  
40.00, 80.00, 160.0, 320.0, 640.0)

Figure 6

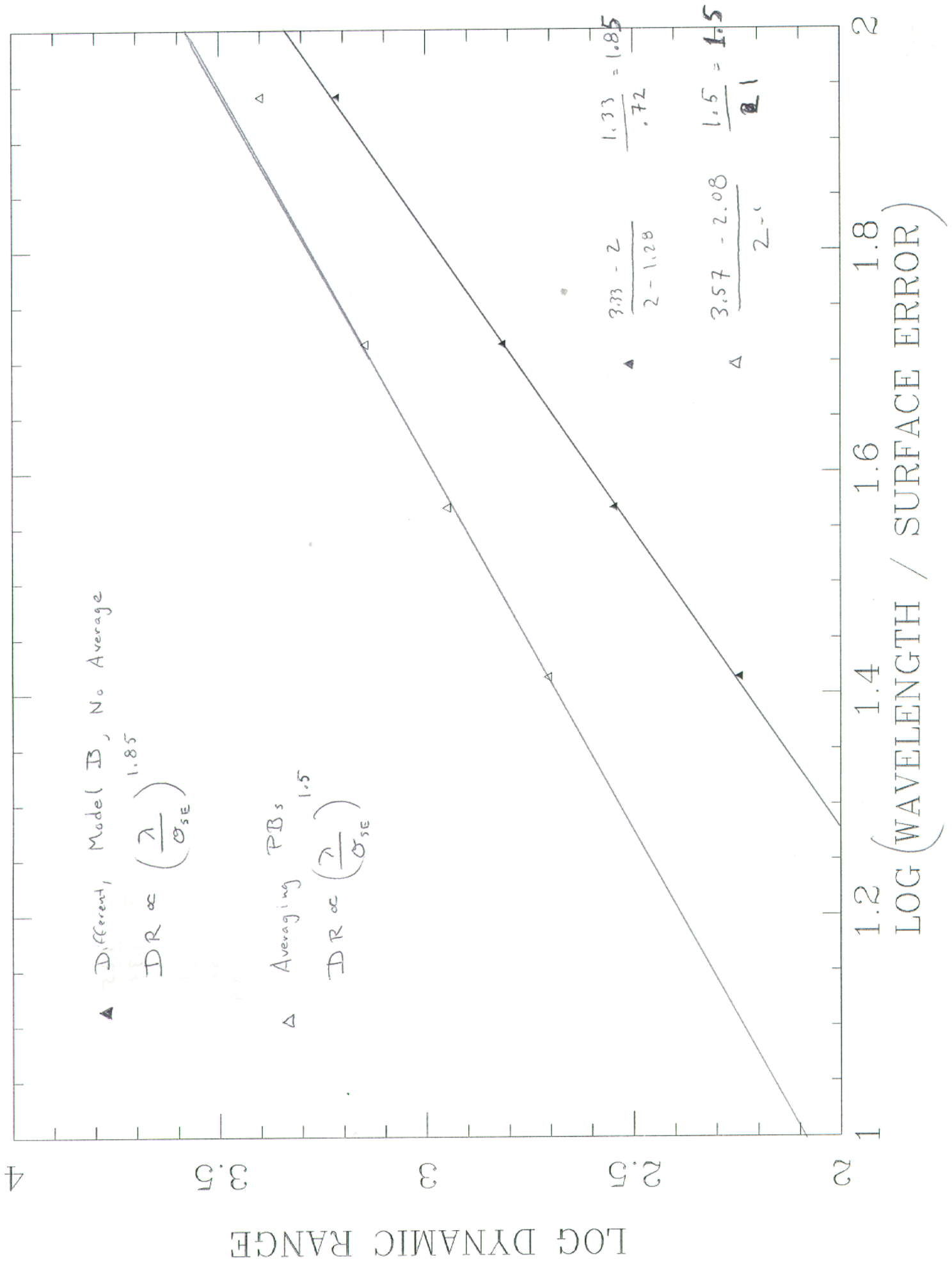


Figure 7

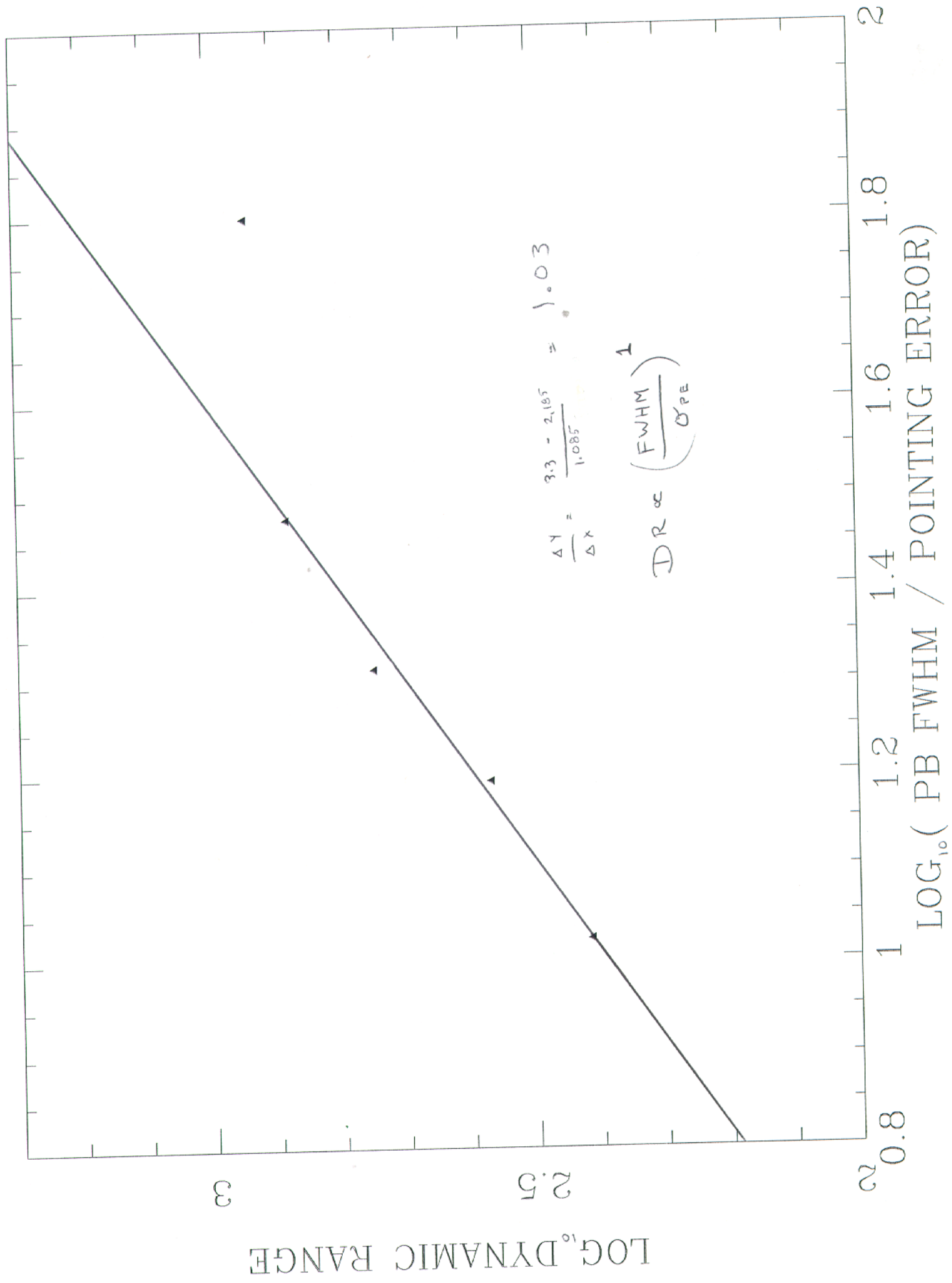
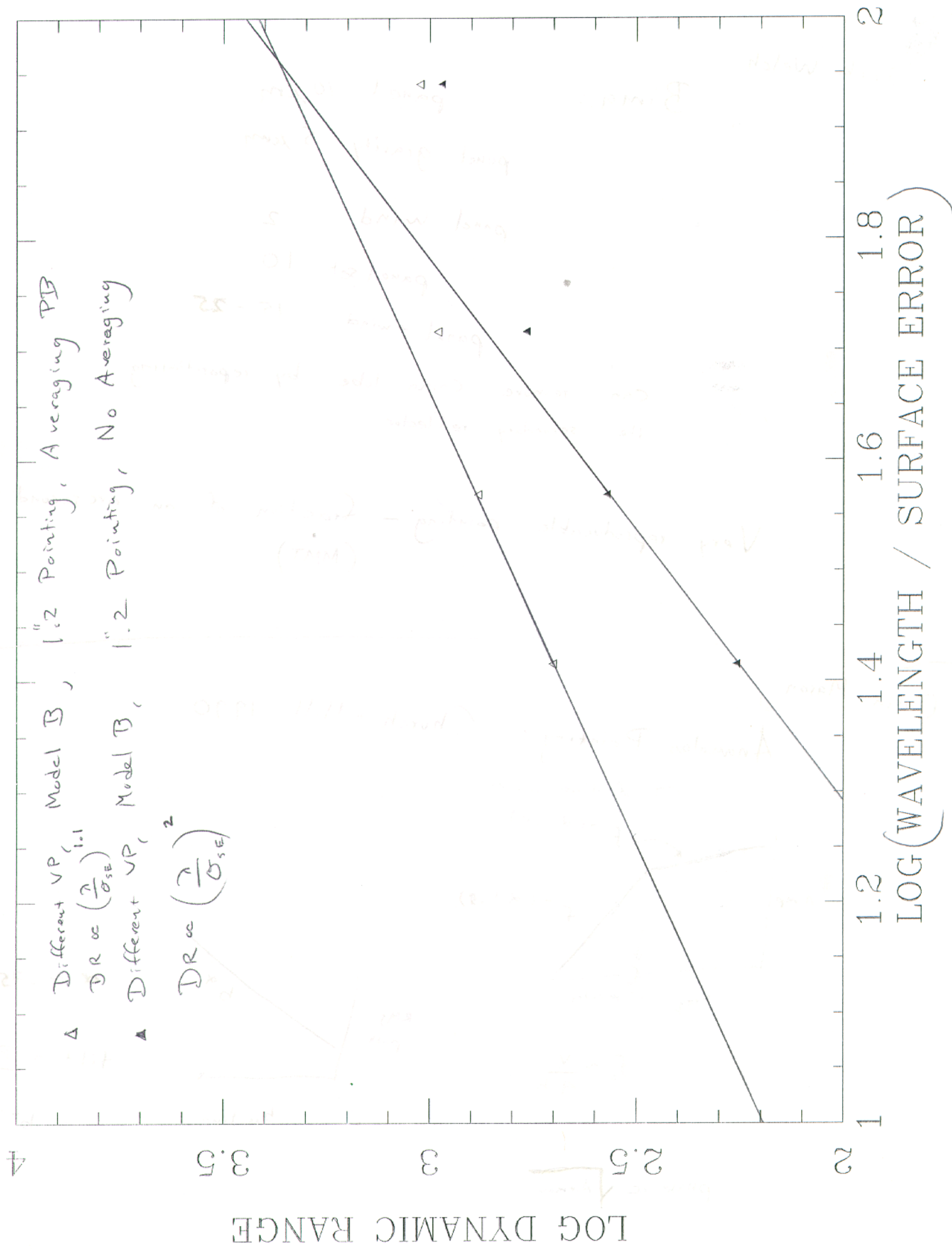




Figure 8



## Figure Captions

Figure 1: An instance of the Model A surface errors.

Figure 2: An instance of the Model B surface errors.

Figure 3: The primary beam obtained from the Model A surface errors scaled to 35 microns ( $\lambda/37$ ).

---

Figure 4: The primary beam obtained from the Model B surface errors scaled to 35 microns ( $\lambda/37$ ).

---

Figure 5: The primary beam obtained from a uniformly illuminated blocked aperture with no surface errors. Agreement with the theoretical PB is excellent.

---

Figure 6: Dynamic Range as a function of  $\lambda/\sigma_{SE}$  for Model B, no pointing errors, with and without PB averaging.

---

Figure 7: Dynamic Range as a function of  $\theta_{FWHM}/\sigma_{PE}$ .

---

Figure 8: Dynamic Range as a function of  $\lambda/\sigma_{SE}$  for Model B, 1"2 pointing errors, with and without PB averaging.